Detailed Investigations of ZnO Photoelectrodes Preparation for Dye Sensitized Solar Cells

6 AUTHORS, INCLUDING:

Renata Seitz
SGL Carbon, Meitingen
21 PUBLICATIONS **421** CITATIONS

SEE PROFILE

Rameez Ahmad
Friedrich-Alexander-University of Erlangen-…
8 PUBLICATIONS **50** CITATIONS

SEE PROFILE

Volodymyr Lobaz
Institute of Macromolecular Chemistry
11 PUBLICATIONS **45** CITATIONS

SEE PROFILE

Wolfgang Peukert
Friedrich-Alexander-University of Erlangen-…
**384** PUBLICATIONS **4,365** CITATIONS

SEE PROFILE

Detailed Investigations of ZnO Photoelectrodes Preparation for Dye Sensitized Solar Cells

Renata Marczak,[†] Fabian Werner,[‡] Rameez Ahmad,[†] Volodymyr Lobaz,[†] Dirk M. Guldi,*[,‡] and Wolfgang Peukert*[,†]

[†]Institute of Particle Technology, Friedrich-Alexander-University Erlangen-Nuremberg, Cauerstr. 4, 91058 Erlangen, Germany

[‡]Department of Chemistry and Pharmacy & Interdisciplinary Center of Molecular Materials (ICMM),
 Friedrich-Alexander-University of Erlangen-Nuremberg, Egerlandstr. 3, 91054 Erlangen, Germany

ABSTRACT: Wurtzite ZnO hexagonal nanopyramids were successfully synthesized in the liquid phase from homogeneous methanolic solutions of zinc acetate and tetramethylammonium hydroxide at an excess of zinc ions. The formation and properties of the nanocrystals were examined as a function of synthesis conditions. No significant influence of the $[Zn^{2+}]/[OH^-]$ ratio was noticed on the final particle size, in spite of increased amounts of OH^- ions, which tend to accelerate the particle nucleation and growth. Nevertheless, the reactant concentration ratio influences the surface properties of the ZnO nanocrystals. Mesoporous ZnO films were prepared by doctor blading ethanolic pastes containing ZnO nanoparticles and ethyl cellulose onto FTO conductive glass substrate followed by calcination. Additionally, the influence of a plasticizer (triacetin)—used during the paste preparation—on the film quality was investigated. A higher content of ZnO nanoparticles and plasticizer in the pastes improved the film quality. Four different temperatures (i.e., 400, 425, 450, and 475 °C) were used for the film calcination and their influence on the structural properties of the films was characterized. In principle, increasing the calcination temperature goes hand in hand with an increase of particle size, as well as the pore diameter and reduction of the surface area. Suitable mesoporous films were employed as photoanodes in dye sensitized solar cells (DSSCs). In order to assess the effect of the varied parameters on complete DSSC devices—using *cis*-diisothiocyanato-bis(2,2′-bipyridyl-4,4′-dicarboxylato) ruthenium(II)bis(tetrabutylammonium (N719) as a sensitizer—incident photon to current efficiency (IPCE) and current voltage measurements were carried out. The IPCE measurements confirmed photoinduced electron injection from the dye, reaching IPCE values up to 76%. Furthermore, current−voltage characteristics of complete cells emphasized the importance of the proper preparation methods and temperatures. These features are important assets for the preparation of nanocrystalline ZnO based photoelectrodes and for improving the DSSC performance.
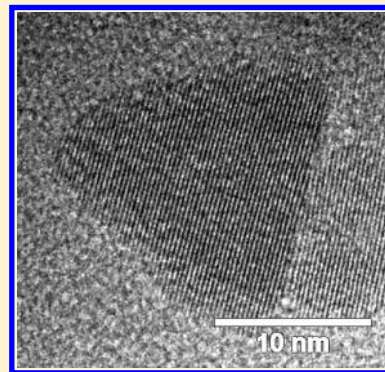
INTRODUCTION

Zinc oxide (ZnO) is an attractive material for a broad range of electronic, optical, and piezoelectric applications due to its direct band gap and excellent thermal, chemical, and structural properties.[1] For example, ZnO has been suggested for use in applications such as solar cells,[2] light emitting diodes,[3] transparent electrodes,[4] sensors,[5] and many other devices.[6] The various applications of ZnO nanoparticles are due to sensitivity to surrounding environments and superior luminescence and photoelectric properties. In particular, the application of ZnO nanoparticles for constructing dye sensitized solar cells (DSSCs)[2a,7] is a point of interest.[2b,d,8] DSSCs are based on photoelectrochemical mesoporous metal oxide electrodes, to which a dye is adsorbed. DSSCs offer a potentially low cost, medium performance alternative to traditional photovoltaic devices. Mostly, titanium dioxide (TiO_2)[2a,7] has been the material of choice and so far has led to the highest overall light conversion efficiencies.[9] However, ZnO has recently been explored as an alternative material for DSSCs, as this wide band gap semiconductor possesses an energy band structure and physical properties similar to those of TiO_2, but has

higher electronic mobility favoring electron transport with reduced recombination loss when used in DSSCs.[2d,8,10] Since DSSCs consist of a combination of several inorganic and organic materials,[2a,7] the properties of each component influence the overall cell efficiency. In short, the cell conversion performance depends on the properties of the porous semiconductor film, the dye molecule, the redox couple, and the solvent in the electrolyte, as well as the characteristic of the counter electrode.[7] In nanocrystalline DSSCs, the porous film consists of a large collection of nanosized particles of a metal oxide interconnected by mesosized pores, deposited onto a conductive surface of a transparent electrode. This porous metal oxide film acts as a high surface area support for the sensitizer, a pathway for electrical current, and a porous membrane for diffusion of the redox couple.[11] In highly porous films (i.e., few micrometers thickness), the available surface area for dye adsorption is enormous, leading to near extinction of

incident light within the spectral range of the sensitizer.[2a,12] To guarantee the regeneration of the oxidized dye, the structure of the pores must permit the penetration of the electrolyte containing the redox couple and enable an effective mass transport of electroactive species by diffusion.[13] Furthermore, the porous films must exhibit interconnected particles, to allow the percolation of injected electrons. The crystallinity of the particles also influences the injection of electrons and their transport through the network of the particles in the film.[12,14]

The broad range of accessible ZnO nanostructures is well reflected in the multitude of different approaches, which have been pursued to construct ZnO based electrodes. In the field of DSSCs, the approaches range from wet chemical synthesis followed by calcinations[15,8b] over low-temperature approaches[15] to templated synthesis.[16a] Various ZnO-based structures, such as core—shell nanowires,[16b] aligned nanorods,[16a,c] hierarchical structures,[17a] and nanoflowers,[17b] have been realized. The best overall efficiencies are reported to be around 5%[18a] utilizing relatively large particles (i.e., diameters of about 150 nm). These large particles have the benefit of directly scattering the light and thereby allowing for broader spectral absorption within the device. However, the large size limits the active surface area at low electrode thicknesses necessary for efficient device design and promotes back scattering directly at the interface between the conducting glass and ZnO.[18a,b] A double layer structure with a light trapping layer on top of a high surface area layer is found to be optimum.[18b]

Different synthesis routes have been developed, including solid-vapor phase thermal sublimation,[19] spray pyrolysis,[20] RF plasma synthesis,[21] sonochemical or microwave-assisted synthesis,[22] and hydrothermal processing.[23] However, wet-chemical synthesis of ZnO is an area of particular interest, since it provides low-temperature, economical ways to produce various ZnO nanostructures.[1,24] Synthesis conditions such as temperature[35] and the overall concentration of the precursors,[24c,e] as well as their concentration ratios,[38] ions present in solution,[39] and solvents,[37] have been shown to influence particle nucleation and growth. Reaction typically starts with the formation of clusters, which react to stable nuclei followed by crystal growth, thus consuming the supersaturation until the cation concentration reaches the solubility of the oxide. Zinc salts suspended in alcohols at elevated temperatures slowly form basic salts with water and complexes with the alcohol molecules.[1,24b] The structures of these depend on the overall humidity and pH in the system.[25a−c] Addition of base triggers dehydration of zinc oxide precursors with oriented attachment of preformed clusters forming ZnO nuclei. The amount of added base influences the dehydration rate and, in turn, the number of nuclei is proportional to the hydroxide concentration. Since 1980, the $[Zn^{2+}]/[OH^-]$ ratios have changed from 1/1.35 to 1/30. The increase of OH^- concentration always leads to the formation of smaller particles, and at ratios above 1/30, no zinc oxide is formed.[25a] Water affects particle growth, mainly by increasing the solubility of zinc compounds and, in turn, accelerating the ripening processes along the c-axis. To this end, upon changing the water content in the system, ZnO nanoparticles with various shapes were obtained, starting from semispheres through rods with different aspect ratios to lamellar hierarchical structures.[25c] Likewise, temperature influences the solubility of ZnO and, as a consequence, formation of rods through ripening seems to happen at elevated temperatures. The hydroxide counterion as well as molecules able to form complexes with

Zn^{2+} are known for selective adsorption on certain crystal planes of growing ZnO particle and, thus, strongly influencing the particle shapes.[26] The well-known process of ZnO rod formation by oriented attachment of nanoparticles, as documented by Weller and co-workers,[24c] was not observed by Cheng and co-workers[25c] in a system containing zinc acetate and tetramethyl-ammonia hydroxide in methanol at a similar temperature. Taking the aforementioned in concert, we reach the conclusion that the complete mechanism of zinc oxide formation is not fully established.

In this paper, we report on a versatile strategy, including a simple colloidal method, to synthesize highly crystalline ZnO nanoparticles from zinc acetate and tetramethylammonium hydroxide in methanol complemented with a simple and reproducible technique to form nanocrystalline porous film and to fabricate DSSC. The overall synthesis procedure of Cheng et al.[25c] was modified in terms of lower reaction temperature and larger $[Zn^{2+}]/[OH^-]$ ratios. The formation and properties of the nanocrystals are discussed as depending on the synthesis parameters such as reaction time and the reactant concentration ratio $[Zn^{2+}]/[OH^-]$. To survey the growth mechanism, we employed X-ray powder diffraction (XRD) to identify the products of the synthesis and finally quantify the particle size in order to study the influence of synthesis conditions on the growth of ZnO nanocrystals. This was complemented by high resolution transmission and scanning electron microscopies (HRTEM and SEM), thermogravimetric analysis (TGA), and attenuated total reflectance Fourier transform infrared spectroscopy (ATR-FTIR).

The aforementioned was completed by using the ZnO nanoparticles as the nanocrystalline electrode material in DSSCs. To this end, ZnO films were fabricated and a detailed investigation of the film properties with respect to their preparation procedure and conditions such as paste composition and concentration, number of layers, or calcination temperature is shown. XRD, SEM, profilometry, and BET sorption measurements were applied to test the film crystallinity, morphology, thickness, and porosity. Finally, the impact of the varied factors on the cell performance is discussed.

■ MATERIALS AND METHODS

Synthesis of ZnO Nanoparticles. All chemicals were analytical grade reagents purchased from commercial sources and used without further purification. The ZnO nanoparticles were prepared by dissolving zinc acetate dihydrate, $ZnAc_2 \times 2H_2O$ (ACS grade, 98.0%, VWR, Germany), in methanol (99.9%, Carl Roth GmbH & Co KG, Germany) at 75 °C. Then, a methanolic solution of tetramethylammonium hydroxide, TMAOH (25% (w/w), Sigma-Aldrich, Germany), was added dropwise under stirring at 250 rpm. Four different concentration ratios $[Zn^{2+}]/[OH^-]$ were studied. The ratio was adjusted to 1/0.5, 1/0.375, 1/0.25, and 1/0.125 while keeping the Zn^{2+} concentration constant at 0.5 mol L^{-3}. The particles were refluxed in their mother liquors up to several days at 75 °C for equilibration. Next, in order to remove remaining salts and the reaction byproduct the ZnO nanoparticles were washed by repeated centrifugation and decantation. The ZnO nanoparticles were then washed with ethanol. Before further characterization, the particles were dispersed in ethanol by sonication for 15 min.

Particle Characterization. Structural analysis of the ZnO nanoparticles was performed in a D8 Advance (Bruker AXS) X-ray diffractometer (XRD) using Cu Kα radiation (0.154 nm). Measurements were done in the range of $28° \leq 2\theta \leq 65°$. High-resolution transmission electron microscopy (HRTEM) images were obtained using a Philips CM 300 UltraTwin microscope with the particles deposited on a

standard copper grid supported carbon film. Scanning electron microscopy (SEM) images were obtained using a Zeiss Gemini Ultra 55 SEM. Samples were prepared by drop casting on silicon wafers. Measurements were carried out at an acceleration voltage of 5 kV in the dark-field mode. Attenuated total reflectance Fourier transform infrared (ATR-FTIR) spectra were recorded on a Varian Excalibur Spectrometer FTS 3100 with a resolution of 2 cm^{-1} under nitrogen flow. Ethanolic suspensions of the nanoparticles were dropped onto the surface of an internal reflection element. Thermogravimetric measurements were carried out using a Q50 Thermoanalyser (TA Instruments, USA). For the measurements, a small amount of powder (about 15 to 20 mg) was heated from room temperature to 600 °C at a constant heating rate of 10 °C min^{-1} under a nitrogen flow of 60 mL min^{-1}.

ZnO Film Preparation. In order to produce ZnO nanoparticles suitable to be used in dye sensitized solar cells, a ratio $[Zn^{2+}]/[OH^-]$ of 1/0.375 was used and the nanocrystals were aged for 3 h. Next, pastes with different weight percentages (wt %) of ZnO nanoparticles were obtained by mixing the nanoparticles with 10% ethanolic solutions of ethyl cellulose (5−15 mPas #46070 and 30−50 mPas #46080, Aldrich, in a 1/1 ratio). The viscosity of the ethyl cellulose was measured by the manufacturer in 5% solution in a mixture of toluene/ethanol (v/v; 80/20) at 25 °C and shear rates of 0.5 and 25 s^{-1} according to ASTM D 445 (DIN 51562). The exact content of the ZnO nanoparticles in the pastes was confirmed by TGA. During the investigation, the weight percentage of ZnO nanoparticles in the pastes varied between 5% and 20%. Moreover, in order to improve the quality of the films the influence of a plasticizer for cellulose, which was triacetin (1,2,3-triacetoxypropan, Sigma-Aldrich, Germany), was also examined. Therefore, 3 wt % of triacetin was added during the preparation of the paste. Then, all the mixtures were slowly stirred at room temperature until the paste became homogeneous and all air bubbles were removed.

Further, the resulting transparent paste was doctor bladed onto TEC 15 F/SnO$_2$ conducting glass substrates (FTO). Both edges of the FTO glasses were covered with a layer of Scotch Magic Tape (approximately 60 μm). A drop of the paste was applied to one of the bare edges of a FTO substrate and flattened with a microscopy glass slide by sliding over the tape-covered edges.[27] After evaporation of the solvent, the tape was removed and the films were slowly heated to their calcination temperature which was held for 10 min. Four different temperatures, i.e., 400, 425, 450, and 475 °C, were used for film calcination.

In order to increase the thickness of the films, three different preparation routes were followed. First, two layers of the tape were applied during a single film deposition. Second, one layer of the tape was utilized and the layer of ZnO paste was dried at 250 °C. After cooling, the second layer of the paste was deposited. Third, the first layer was calcinated at 450 °C for 15 min, cooled down, and coated with the second layer of the ZnO paste. Subsequently, all the films were calcinated at 450 °C for 10 min. In all cases, two different ZnO nanoparticle concentrations in the pastes, that is, 5 and 20 wt %, were tested for film preparation. 3 wt % of triacetin was added to both of them.

ZnO Film Characterization. The morphology of the films was examined by scanning electron microscopy (SEM). The thickness of the films was measured by profilometry using a Dektak II Profilometer. Moreover, the crystallite size of the particles in the films was determined according to the Debye−Scherrer equation[30] applied to the XRD patterns recorded with a D8 Advance (Bruker AXS) X-ray diffractometer (XRD). Furthermore, the surface area and the average pore diameter of about 50 mg samples scraped off the substrate were obtained by a gas adsorption method using a BET adsorption−desorption isotherm (N$_2$ as adsorbate, Quantachrome Nova 4000e).

Device Fabrication. Nanocrystalline ZnO coated FTO conducting glass slides with an active area of 1 cm^2 were sensitized with a dye molecule, a commercially available Ruthenizer 535-bisTBA (N719, *cis*-diisothiocyanato-bis(2,2′-bipyridyl-4,4′-dicarboxylato)

ruthenium(II)bis(tetrabutylammonium). Therefore, the ZnO films were immersed for 1.5 h in a 10^{-4} mol L^{-3} ethanolic solution of the dye at 50 °C and rinsed with the solvent to remove any ungrafted dye molecules.[28a]

DSSCs have been fabricated from these slides. For counter electrode fabrication, uncoated conducting glass slides were cut into pieces and either one or two holes of 1 mm^2 were drilled at the edge of the active area. A thin film of H$_2$PtCl$_6$ (0.01 mol L^{-3} in ethanol) was spread over the conducting glass electrode, which was allowed to dry in air prior to firing at 380 °C for 20 min. The ZnO and platinum counter electrode were then sealed together with a transparent film of Surlyn 1472 (Dupont) cut as a frame around the nanocrystalline ZnO film. A solution of 0.6 mol L^{-3} 1-methyl-3-propylimidazolium iodide (MPII), 0.03 mol L^{-3} I$_2$, in methoxyacetonitrile was employed as electrolyte. The electrolyte was introduced through the hole drilled in the counter electrode and immediately sealed.

Photoelectrochemical Characterization. Photocurrent measurements were carried out using a Keithley Sourcemeter 2400 during illumination. A collimated light beam from an adjustable 1000 W xenon arc lamp was used for UV and vis illumination closely matching AM 1.5 conditions at 1 sun. When white light was used, a 350 nm cutoff filter was introduced in the light beam. When recording the photoaction spectrum, a B&M Spektronik grating monochromator was introduced into the path of the excitation beam for selecting the required wavelengths. All measurements were performed after subtracting stable dark current. The incident photon-to-current conversion efficiency (IPCE) defined as the number of electrons collected per incident photon was determined from short-circuit photocurrent measurements at different wavelengths. All experiments were performed at room temperature.

■ DISCUSSION

ZnO Nanoparticle Synthesis and Characterization. The ZnO nanoparticles were synthesized by means of precipitation from methanolic solutions containing zinc acetate and tetramethylammonium hydroxide at 75 °C under vigorous stirring. The synthesis reported by Cheng et al.[25c] was modified with respect to larger $[Zn^{2+}]/[OH^-]$ ratios and lower temperatures. Both factors are expected to improve the crystallinity of the nanoparticles and avoid the formation of rods. The nanoparticle suspensions were aged under reflux and examined by XRD to follow the progress of the crystal growth. Figure 1 shows the XRD patterns of the samples recorded after different refluxing times. During the first 10 min, before TMAOH solutions were added, zinc acetate was the only crystalline phase that was present in the system (Figure 1a). At early stages after the addition of TMAOH (Figure 1b), no crystalline peaks related to either zinc acetate or ZnO were discernible. Nevertheless, some crystalline structures, which correspond to zinc oxide precursors,[1] are present in the system. Upon prolonged refluxing (Figures 1c−g), diffraction peaks evolved, which are assigned to the standard hexagonal phase of ZnO with a wurtzite structure (reported in JCPDS card no. 36−1451). Another observation is that at shorter reaction times (Figure 1c−e) the ZnO peaks are broad and the (002) reflection is overlapping with the (101) reflection due to small crystal sizes. Upon aging (Figure 1f and g), the diffraction peaks intensify and narrow, while the (002) diffraction emerged as a clear peak, which indicates increased crystallinity. Important during this stage is the lack of impurity peaks in the XRD patterns. Generally, the nuclei formation and the growth of ZnO nanoparticles in alkaline methanol solutions is complex. A dynamic balance prevails between temperature-sensitive processes such as dissociation of the precursors (i.e., enabling the nucleation), the growth of the nuclei, and their concomitant
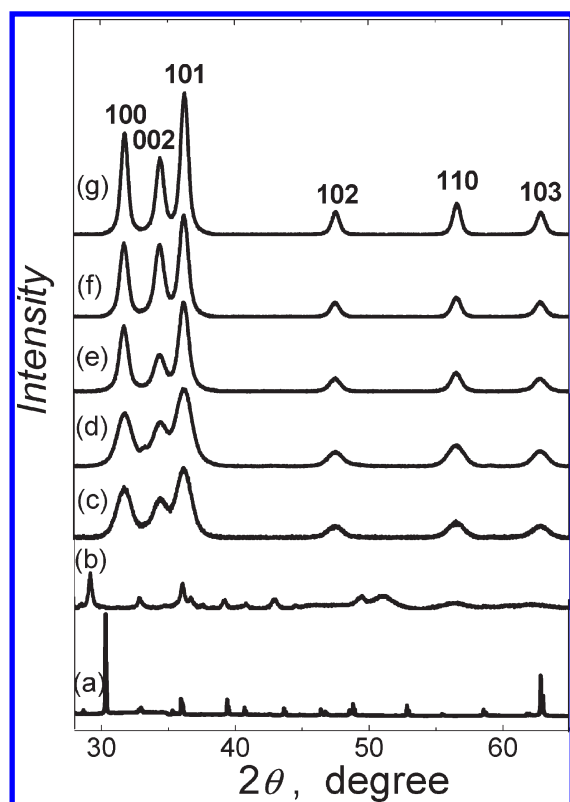
Figure 1. XRD patterns of ZnO nanoparticles synthesized in methanol with the reactant ratio $[Zn^{2+}]/[OH^-]$ of 1/0.5 and refluxed at 75 °C for (a) 10 min (b) 0.5 h, (c) 2 h, (d) 3 h, (e) 4 h, (f) 24 h, and (g) 48 h.

Figure 2. Average coherence diameters of ZnO nanoparticles synthesized in methanol with the reactant ratio $[Zn^{2+}]/[OH^-]$ of 1/0.5 (black squares and line), 1/0.375 (red triangles and line), 1/0.25 (green circles and line), and 1/0.125 (blue rhombus and line) monitored as a function of the refluxing time at 75 °C and delivered from the FWHT of the (a) 100, (b) 002, and (c) 101 peaks of XRD patterns according to the Debye–Scherrer equation.[30]

dissolution (i.e., Ostwald ripening). In particular, the reaction involves the dissociation of zinc acetate, formation of preformed clusters, and ZnO nucleation and growth. At short refluxing time, before the addition of a base no crystalline phases, besides zinc acetate, were observed. The added hydroxide nourishes the reaction of zinc acetate with hydroxyl groups, followed by the dehydration of the formed precursors, which altogether enable the ZnO nucleation and growth.

Regarding the precipitation of ZnO in the presence of LiOH as a hydroxide source, the early stages of ZnO nanoparticle formation are limited by the chemical reaction rather than by diffusion.[29,38] Thus, the amounts of the hydroxide used, e.g., reaction stoichiometry $([Zn^{2+}]/[OH^-])$, are expected to play an important role in the particle formation. To confirm this assumption, we focused on four different $[Zn^{2+}]/[OH^-]$ ratios (i.e., 1/0.5, 1/0.375, 1/0.25, and 1/0.125) and monitored the progress of the particle formation during ripening by XRD. We found that the rate of particle formation depends strongly on the amount of hydroxide. It was possible to detect ZnO nanoparticles after about 60, 90, 180, and 300 min of the reaction for $[Zn^{2+}]/[OH^-]$ ratios of 1/0.5, 1/0.375, 1/0.25, and 1/0.125, respectively. Furthermore, crystallite diameters of the nanoparticles were calculated from the (100), (002), and (101) peaks of the XRD patterns according to the Debye–Scherrer equation.[30] From Figure 2, which depicts the changes of the diameter as a function of the aging time, we deduce that increasing amounts of OH^- ions indeed accelerate the particle nucleation and, in turn, crystal growth. On the other hand, the final size and morphology are strongly affected by the diffusion limited ripening during the final stages of the reaction. The ripening kinetics depends on the
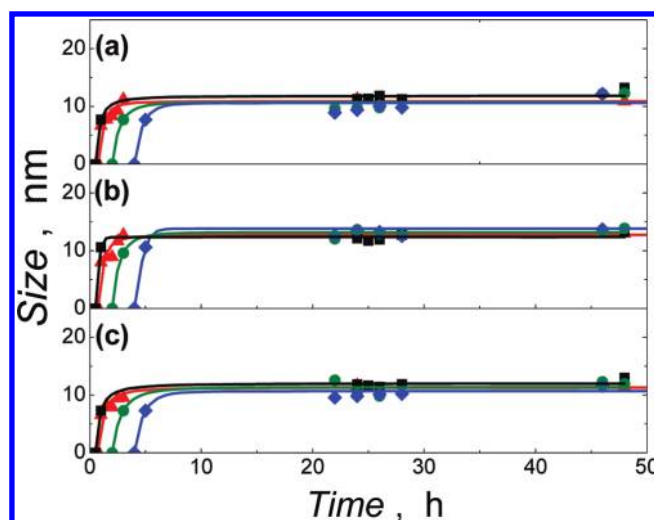
ZnO solubility and other zinc containing species. Therefore, the amount of water is essential, since water is known to be a better solvent for zinc oxide than methanol. The calculated amount of water in the system is 2.4 vol % This correlates with "low water content" in the work of Cheng et al.[25c] We believe that in our case the interaction of zinc acetate with the present amount of water has a weak impact on the nucleation due to the short reaction times before the addition of the hydroxide. In fact, the detectable amounts of zinc oxide precursors were not observed by XRD (Figure 1a). Nevertheless, after a certain reaction time only a ZnO crystalline phase is detected. The latter documents the full transformation of all precursors into zinc oxide crystals. From this moment on, the particle size grows by slow diffusion controlled long-term ripening. Importantly, as is seen in Figure 2, no significant influence of $[Zn^{2+}]/[OH^-]$ ratios on the final particle size is noticed. It is noteworthy that no rods are formed, contrary to the results reported by Cheng et al.,[25c] mainly because of our sufficiently lower temperature. Additionally, growth processes are terminated due to the adsorption of acetate and tetramethylammonium ions, as well as solvent molecules on polar crystal planes of growing ZnO, thus passivating them. The nanoparticle size in the system, which evolves according to the long-term ripening process, is rather a function of overall Zn^{2+} concentration in the system than of the $[Zn^{2+}]/[OH^-]$ ratio. The adsorbed ions stabilize the ZnO particles against aggregation. Therefore, the oriented aggregation of nanoparticles including the formation of rods, as described by Weller et al.,[24c] for a system of ZnO from zinc acetate upon addition of potassium hydroxide was not observed in our system.

The properties of ZnO based DSSCs greatly depend on the surface characteristics of the nanoparticles. Therefore, to examine and to compare the surface properties of nanoparticles synthesized with different tetramethylammonium hydroxide concentrations all of the methanolic suspensions were aged for 48 h to afford nanocrystals of comparable diameters. First, compositional information about the species present at the
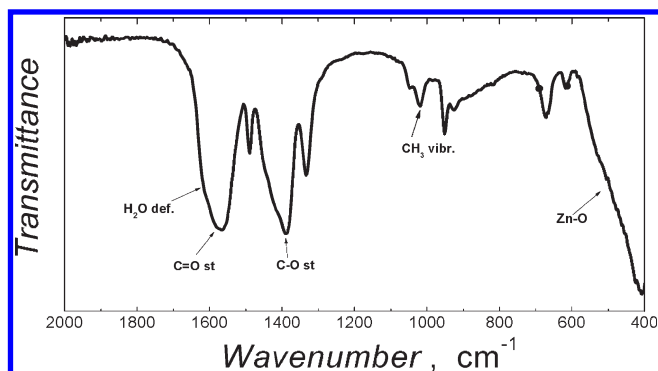
Figure 3. ATR FTIR spectra of ZnO nanoparticles synthesized with the reactant ratio $[Zn^{2+}]/[OH^-]$ of 1/0.5 and refluxed in methanol for 48 h at 75 °C.

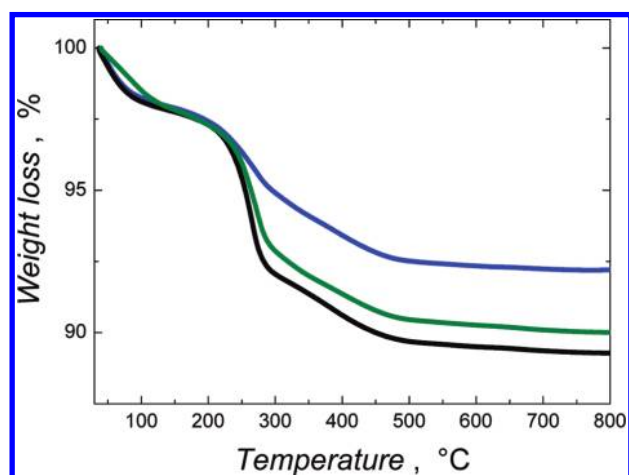**Figure 4.** TGA Curves of ZnO nanoparticles synthesized with the reactant ratio $[Zn^{2+}]/[OH^-]$ of (a) 1/0.5 (black line), (b) 1/0.25 (green line), and (c) 1/0.125 (blue line) and refluxed in methanol for 48 h at 75 °C.

Figure 5. (a) SEM and (b) HRTEM images of ZnO nanoparticles.

particle surface was gathered from infrared spectroscopy. ATR FTIR spectra, as shown in Figure 3, reveal that the ZnO particle surface is covered with acetate and tetramethylammonium groups. The broad asymmetric peaks in the ranges 1550−1650 and 1370−1460 cm^{-1} are attributed to overlapping C═O and C−O stretching vibrations,[31] which are characteristics of acetate binding via three possible structures, namely, monodentate, bidentate, and bridging motifs. It is, however, impossible to resolve and to identify the respective bands due to the overall overlap. The signature at 1650 cm^{-1}, present as a shoulder, is often attributed in the carboxylic acid−carboxylate−water systems to the deformation vibration of water molecules.[32] Furthermore, the weak bands at 1050 cm^{-1} are ascribed to rocking vibrations of the methyl groups of the tetramethylammonium groups on the particle surface.[33] The intensive bands below 500 cm^{-1} are attributed to the vibrational modes of Zn−O.[34]

Next, in order to obtain quantitative information about the adsorbates at the particle surface thermogravimetric analysis (TGA) was employed. Figure 4 displays changes of the sample weight during heating. TGA analyses point to three distinctive stages of weight loss. In particular, weight losses below 170 °C correlate to the evaporation of solvent—methanol and ethanol—that is needed for particle preparation and that is still left in the samples. The weight loss stages above 170 °C are attributed to
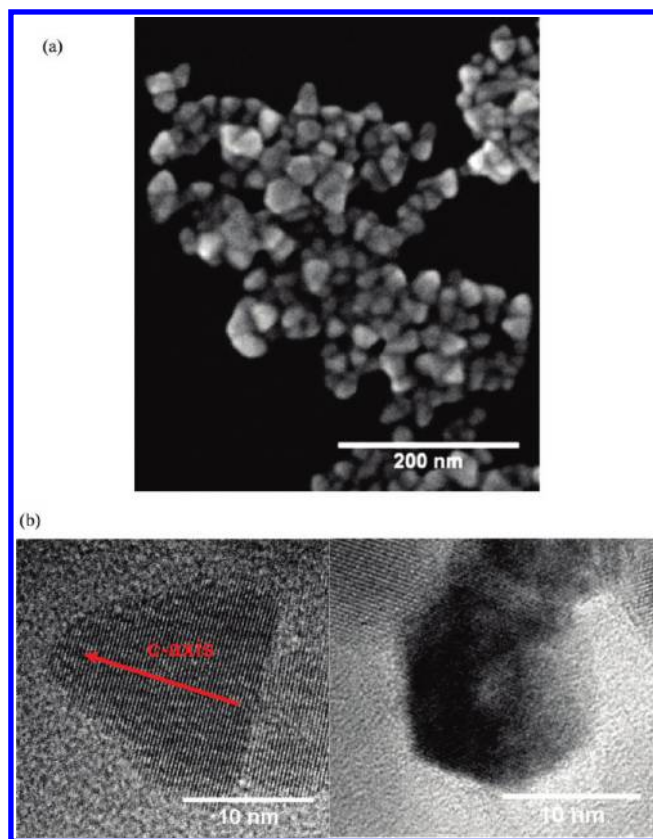
the chemisorbed organic groups on the surface of the ZnO nanocrystals, which originate from the precursors. It was proven elsewhere[35a,36] that the liberation of monodentate acetate from the surfaces starts at temperatures above 200 °C; therefore, the sharp weight decrease between 200 and 280 °C is identified with/corresponds to the tetramethylammonium and acetate mixture, whereas the weight loss between 300 and 450 °C is due to the degradation of acetate groups strongly bound to the particle surface.[35a,36] After following these steps, the weight levels off at a constant final value.

The amount of tetramethylammonium and monodentate acetate rises significantly as a function of tetramethylammonium hydroxide concentration. In contrast to the report by Sakohara et al.,[31] which shows an increase of the monodentate acetate fraction at the expense of strongly bound acetates with lowering $[Zn^{2+}]/[OH^-]$ ratio, we observe a constant amount of strongly bound acetate in all of the samples. The fact that the zinc acetate concentration was kept constant and tetramethylammonia hydroxide varied leads us to conclude that different amounts of tetramethylammonium are adsorbed at different $[Zn^{2+}]/[OH^-]$ ratios, while the amount of acetate is constant.

In addition, the ZnO nanoparticle morphology was studied by means of scanning electron and high resolution transmission microscopies (SEM and HRTEM). No significant impact of the $[Zn^{2+}]/[OH^-]$ ratio on the final particle shape has been observed. Figure 5a shows a SEM image, which illustrates the general morphology of as-prepared ZnO nanocrystals, of hexagonal nanopyramids. This pyramidal shape and their crystallinity were confirmed by HRTEM images presented in Figure 5b. Since the sizes seen in the SEM images and the crystallite size obtained from HRTEM and XRD measurement are in very good
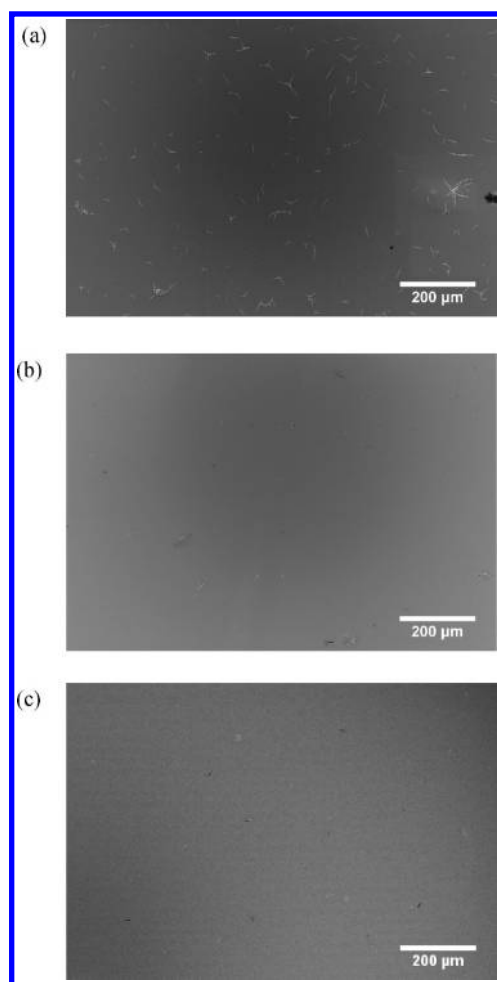
Figure 6. SEM images of ZnO films prepared from the pastes containing (a) 5 wt % and (b) 20 wt % of ZnO nanoparticles and (c) 20 wt % of ZnO nanoparticles with 3 wt % of triacetin.

Figure 7. Thickness of ZnO films (1 layer) as a function of the ZnO content in the paste prepared without plasticizer (green circles and line) and with 3 wt % of triacetin (blue squares and line).

agreement, monocrystallinity of the particles is assumed. In general, the shape of particles is determined by the surface energies of the different crystal planes. Structurally, the wurtzite ZnO crystal is described as a number of alternating planes composed of 4-fold tetrahedrally coordinated O^{2-} and Zn^{2+} ions stacked alternatively along the c-axis.[26] Thus, oppositely charged ions produce positively charged Zn and negatively charged O {001}-surfaces, resulting in a dipole moment normal to this surface and spontaneous polarization along the c-axis, as well as a divergence in surface energy. Besides the {001} polar planes, ZnO has other typical polar surfaces: the {101}-surfaces.[26a] As a matter of fact, polar surfaces are energetically unfavorable and are unlikely to be the exposed surfaces. During crystal growth, polar planes are the faster growing surfaces due to their high surface energies. They exhibit small facets or even disappear in the final shape of the crystal. Nevertheless, the surface energy of such polar planes could be reduced by compensating the surface charge with the passivating reagents such as tetramethylammonium ions, acetate, or the polar solvent used during the synthesis.[26a,37] Due to strong electrostatic interactions between the ions and the polar surfaces, the surface energies of the polar planes decrease in comparison to the other crystal faces. From the latter, we conclude that an unusually slow growth rate for these polar planes evolves. Therefore, the {001} and {101} polar surfaces are those
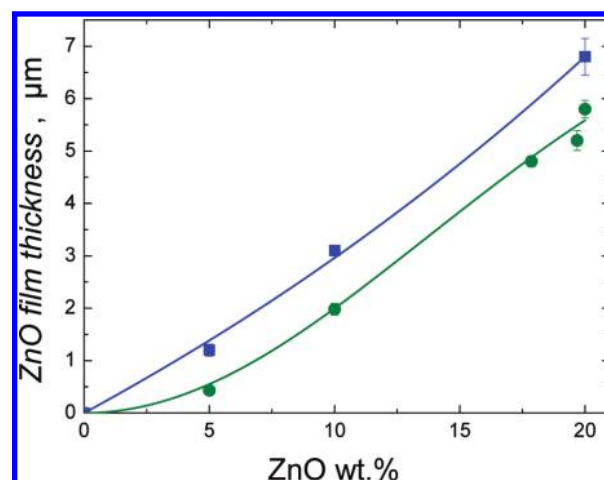
that are exposed and those that facilitate the formation of hexagonal pyramid structures.

ZnO Films Preparation and Characterization. Since the DSSC light-to-energy conversion performance depends on the properties of the porous semiconductor film,[7] the understanding and control of the film properties is a point of our interest.[2b,d,8a] In our study, we focus on the optimization of the ZnO mesoporous film preparation procedure that relates to an enhancement of the cell performance. We have varied in our study only the ZnO concentration and the preparation methods of mesoporous films, while all of the remaining parameters were kept constant. Moreover, standard materials were used for the DSSC preparation. Initially, the morphology of the resulting ZnO films was examined by SEM. The presence of cracks reduces the film adhesion to the conductive substrates and renders it fragile and difficult to handle. Figure 6 shows the SEM images of films prepared from a paste containing 5 wt % (Figure 6a), 20 wt % of the ZnO nanoparticles (Figure 6b), and 20 wt % of the ZnO nanoparticles and the plasticizer (Figure 6c). From these images, it becomes evident that lower nanoparticle amounts in the paste lead to cracked films. The formation of cracks is rationalized on the basis of inducing tension cracks on the film surface due to reducing the paste volume and due to evaporating the solvent during calcination. The presence of cracks reduces the film transparency and their adhesion to the conductive substrates. The increase of the ZnO content in the pastes improves the quality of the films, since less solvent volume evaporates. However, the presence of the plasticizer evokes no further enhancement on the film morphology (Figure 6c).

The film thickness was chosen as the next parameter for optimization, as it is decisive for the sufficient adsorption of the dye, as thicker films relate to larger active surface areas.[2d] The film thickness at various concentrations of ZnO nanoparticles in the pastes was measured by profilometry—see Figure 7. Accordingly, the thickness rises notably from about 0.4 μm for 5 wt % of ZnO nanoparticles up to about 5.8 μm for 20 wt % of ZnO nanoparticles present in the pastes. It is noteworthy that the addition of triacetin further increases the film thickness due the stabilizing function of the plasticizer. As a result, thicknesses of about 1.2 and 6.8 μm were determined for 5 and 20 wt % of ZnO nanoparticles with 3 wt % of triacetin, respectively.
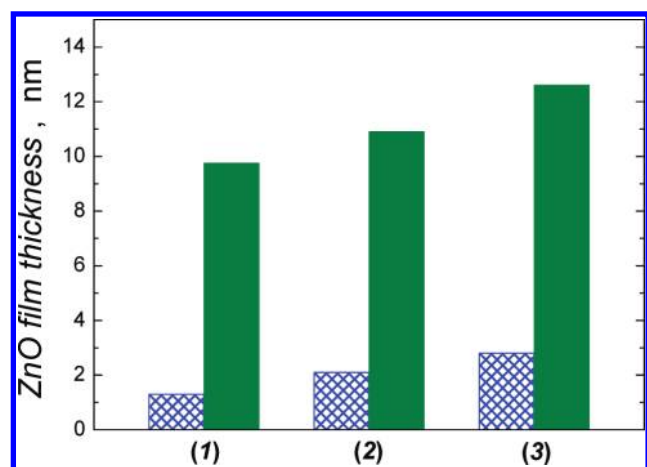
Figure 8. Thickness of ZnO films fabricated from pastes containing 5 wt % of ZnO nanoparticles with 3 wt % of triacetin (blue checked) and 20 wt % of ZnO nanoparticles with 3 wt % of triacetin (green solid) by using different preparation procedures: (1) applying simply two layers of the tape; (2) one layer of the tape was utilized and the film was dried at 250 °C and after cooling down the second layer of the paste was deposited; and (3) the first layer was calcinated at 450 °C, cooled down, and coated by a second layer of the paste.

In order to further improve the thickness of the ZnO films, the number of deposited layers was increased to two in three different preparation routes. First, simply two layers of the tape were applied during a single film deposition. Second, one layer of tape was utilized, but ZnO paste layer was dried at 250 °C, and after cooling, the second layer of the paste was deposited. Third, the first layer was calcinated at 450 °C, cooled down, and coated with the second layer of the ZnO paste. Subsequently, all the films were calcinated at 450 °C. In all cases, two different ZnO nanoparticle concentrations in the pastes, that is, 5 and 20 wt %, were tested for the film preparation. 3 wt % of triacetin was added to both of them. Figure 8 shows that the preparation procedure affects the film thickness. In particular, the thickest films with a thickness of 12.6 μm were fabricated according to the third route. Thus, in the forthcoming film preparations this procedure was used and only the calcination temperature was changed.

The calcination is carried out to form porous ZnO films with particle surfaces, that are suitable for dye adsorption. As is seen from Figure 4, all organic substances are completely liberated from the surface of ZnO nanoparticles above 450 °C. Sintering of ZnO nanoparticles starts at temperatures above 400 °C. On the other hand, electron transport to the FTO depends on the quality of crystallinity and on the intergrain boundaries. The crystalline necking, that is the interconnection of particles, enhances percolation. Thus, the optimal calcination temperature represents the compromise between the complete removal of organic species from ZnO surface, accompanied with enhanced crystallinity, and the reduction of film surface area together with porosity. Four different temperatures (i.e., 400, 425, 450, and 475 °C) were used for the film calcination. The influence of the latter on the structural properties of the films was tested by XRD and SEM. The XRD patterns of the nanostructured films, which are presented in Figure 9, demonstrate that ZnO hexagonal wurtzite structure is preserved during the calcination. To this end, we calculated the average diameter of the nanoparticles constituting the films with the Debye–Scherrer equation.[30] Table 1 lists the corresponding values. Here, the diameter, which
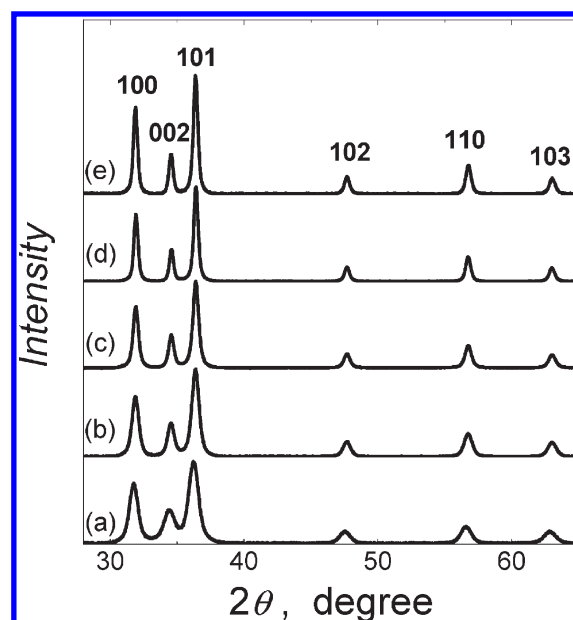

Figure 9. XRD patterns of ZnO films prepared from a paste containing 20 wt % of ZnO nanoparticles with 3 wt % of triacetin (2 layers, third preparation route) (a) not calcinated (the diameter was of 10.1 nm) and calcinated at (b) 400 °C, (c) 425 °C, (d) 450 °C, and (f) 475 °C.

was 10.1 nm for the as-prepared ZnO nanoparticles, increased up to 14.2, 17.9, 22.5, and 22.0 nm when calcinated at 400, 425, 450, and 475 °C, respectively. In addition, the SEM images, which are presented in Figure 10, show that all the films prepared at different temperatures exhibited a porous structure. It is also clearly shown that the particle size increases with temperature and that the structure of the film densifies. More details (i.e., specific surface area and average pore size) about the film porosity were obtained from analyzing the BET nitrogen adsorption isotherms—see Table 1. Our results indicate the decrease of the film thickness and surface area, as well as the increase of pore diameter as function of calcination temperature. Thus, for the preparation of DSSC electrodes the calcination was performed at different temperatures between 400 and 475 °C.

Photophysical Characterization of DSSCs. To assess the effect of the aforementioned optimized parameters on complete DSSC devices, IPCE and current voltage measurements were carried out. The IPCE spectra, which are shown in Figure 11, follow the trend expected for transparent films. To this end, the absorption spectrum of the N719 dye is reproduced with a maximum around 535 nm. Moreover, the absorption band is rather narrow due to the lack of scattering within the layer. Additionally, the influence of the calcination temperature already observed in the BET, SEM, and XRD measurements is confirmed. In terms of efficiency, it is not the film with the highest surface area which shows the highest efficiency. Processes in complete cells are more interdependent on all parameters. For example, the benefits from very high surface areas of samples that were calcinated at 400 °C is compensated by fewer crystalline necking structures—compare the crystallite size listed in Table 1. Thus, the highest IPCE values of up to 76% are observed when the films are calcinated at 425 °C. On the contrary, the values are below 50% for all the other temperatures. Values obtained from current voltage measurements are collected in Table 2. It can be seen that the effect of different temperatures is expressed most

Table 1. Properties of Films Calcinated at Different Temperatures[a]

temperature °C	crystalline size[b] nm	thickness[c] μm	surface area[d] $m^2\,g^{-1}$	pore volume[d] $cc\,g^{-1}$	pore diameter[d] nm
400	14.2	9.5 ± 0.1	48.81	0.206	13.25
425	17.9	8.9 ± 0.3	31.26	0.132	19.43
450	22.5	8.3 ± 0.2	34.47	0.161	18.82
475	22.0	8.2 ± 0.2			

[a] Average crystalline size of non-calcinated ZnO nanoparticles was 10.1 nm.[b] [b] Delivered from patterns according to the Debye−Scherrer equation.[30] [c] Obtained by profilometry. [d] Obtained by a gas adsorption method using a BET adsorption−desorption isotherm (N$_2$ as asorbate).
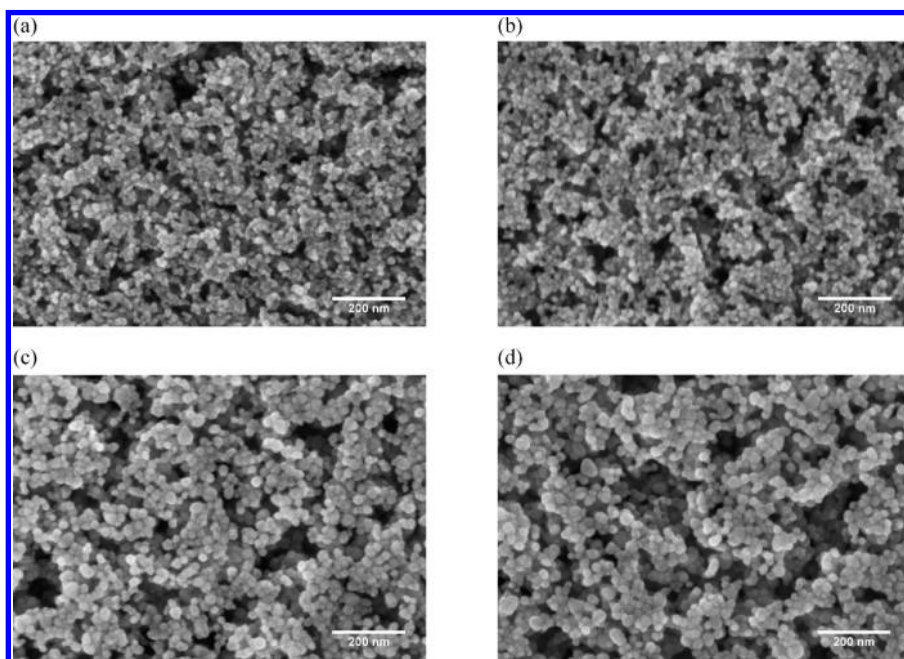

Figure 10. SEM images of ZnO films prepared from a paste containing 20 wt % of ZnO nanoparticles with 3 wt % of triacetin (2 layers, third preparation route) and calcinated at (a) 400 °C, (b) 425 °C, (c) 450 °C, and (d) 475 °C.
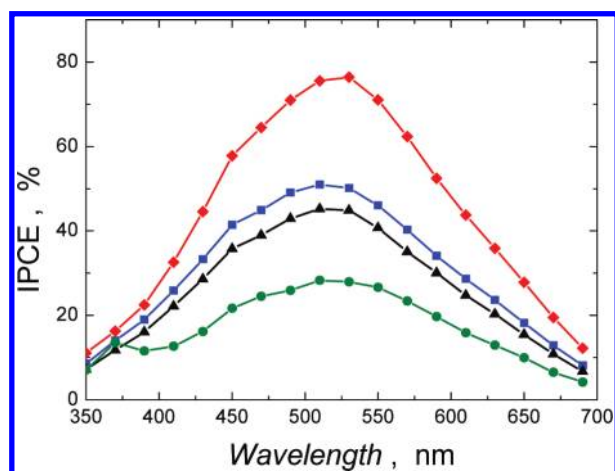

Figure 11. IPCE spectra of ZnO films calcinated 400 °C (green circles and line), 425 °C (red rhombus and line), 450 °C (blue squares and line), and 475 °C (black triangles and line) and sensitized with N719.

Table 2. Summary of Device Characteristics of DSSCs under AM1.5 Illumination at 100 mW/cm^2 Prepared with ZnO Electrodes Calcinated at Different Temperature

temperature °C	I_{sc} (mA cm^{-2})	V_{oc} (V)	FF	η (%)
400	1.72	0.65	0.33	0.37
425	4.98	0.64	0.33	1.07
450	3.83	0.68	0.30	0.78
475	3.79	0.67	0.30	0.76

(FF) and open circuit voltage (V_{oc}) remain constant, emphasizing the comparability of the cells calcinated at different temperatures.

With the missing light trapping mechanisms, that is, anti-reflection coating, scattering layer, and reflection layer, taken into account, the maximum IPCE value of 76% is rather impressive. Electron collection has been effectively optimized by means of improving the electrode structure and its interplay of structure, surface area, porosity, and thickness.

clearly in the changes in short circuit current (I_{sc}) and overall efficiency (η). Here, the trend observed in the IPCE measurements is confirmed. It is important to notice that the fill factor

■ CONCLUSIONS

A wet chemical synthesis of well-defined crystalline ZnO nanoparticles with a hexagonal pyramidal shape is presented. The particle shape evolves from the growth mechanism in the

presence of passivating reagents such as tetramethylammonium ions, acetate, or polar solvents lowering the surface energy of the polar surfaces. Moreover, the particle formation kinetics is governed by the reaction stoichiometry $[Zn^{2+}]/[OH^-]$, while the final particle size and shape remain constant and independent. Likewise, the concentration ratio influences only the surface properties of the nanoparticles.

Furthermore, the simple and economical preparation of mesoporous ZnO films suitable as photoelectrodes in DSSCs is demonstrated. Both a higher content of ZnO nanoparticles in the pastes and the addition of plasticizer lead to thicker films. Thicker films are also realized by increasing the number of layers and the approach of their deposition. The increase of ZnO content in the pastes improves the quality of the films. However, no further enhancement is seen in the presence of the plasticizer.

Subsequently, the films are sensitized with *cis*-diisothiocyanato-bis(2,2′-bipyridyl-4,4′-dicarboxylato) ruthenium(II)bis-(tetrabutylammonium (N719) and the impact of the film preparation conditions on DCCSs performance is discussed. Incident photon to current efficiency (IPCE) measurements confirm a photoinduced electron injection from the dye into ZnO. It is important that the IPCE values follow the temperature dependence trend as they increase up to 76%. Taking the absorption of the FTO glass into account, this is an almost complete conversion of photons reaching the active layer into electrons. However, the rather modest conversion efficiencies are attributed to the transparent nature of the films. In particular, the absence of scattering suggests that efficiencies might be improved by the incorporation of scattering or reflective layers. Furthermore, current−voltage characteristics of complete cells corroborated the results obtained from IPCE measurements.

The preparation conditions indicate that an annealing temperature of 425 °C is an optimum between surface area, crystalline necking of particles, and film thickness. The results presented in this study open the way toward the development in the nanocrystalline photoanodes preparation in order to enhance the DSSC performance.

■ AUTHOR INFORMATION

Corresponding Author

*Prof. Dirk M. Guldi, Department of Chemistry and Pharmacy, Friedrich-Alexander-University Erlangen-Nuremberg, Egerlandstr. 3, 91058 Erlangen, Germany; phone +49 9131 8527341, fax +49 9131 85 28307, email guldi@chemie.uni-erlangen.de. Prof. Wolfgang Peukert, Institute of Particle Technology, Friedrich-Alexander-University Erlangen-Nuremberg, Cauerstr. 4, 91058 Erlangen, Germany; phone +49 9131 8529400, fax +49 9131 85 29402, email W.Peukert@lfg.uni-erlangen.de.

■ ACKNOWLEDGMENT

■ REFERENCES

(1) Spahnel, L. *J. Sol-Gel Sci. Technol.* **2006**, *39*, 7–24.

(2) (a) O'Regan, B.; Grätzel, M. *Nature* **1991**, *353*, 737–739. (b) Quintana, M.; Edvinsson, T.; Hagfeldt, A.; Boschloo, G. *J. Phys. Chem. C* **2007**, *111*, 1035–1041. (c) Redmond, G.; Fitzmaurice, D.; Grätzel, M. *Chem. Mater.* **1994**, *6*, 686–698. (d) Zeng, L.; Dai, S.; Xu, W.; Wang, K. *Plasma Sci. Technol.* **2006**, *8*, 172–176.

(3) Colvin, V. L.; Schlamp, M. C.; Alivisatos, A. P. *Nature* **1994**, *370*, 354–357.

(4) Duran, P.; Capel, F.; Tartaj, J.; Moure, C. *Adv. Mater.* **2002**, *14*, 137–141.

(5) (a) Rout, C. S.; Raju, A. R.; Govindaraj, A.; Rao, C. N. R. *Solid State Commun.* **2006**, *138*, 136–138. (b) Yang, M.; Wang, D.; Peng, L.; Zhao, Q.; Lin, Y.; Wei, X. *Sens. Actuators, B* **2006**, *117*, 80–85.

(6) (a) Johnson, J. C.; Yan, H.; Schaller, R. D.; Haber, L. H.; Saykally, R. J.; Yang, P. *J. Phys. Chem. B* **2001**, *105*, 11387–11390. (b) Zhang, X. T.; Liu, Y. C.; Zhang, L. G.; Zhang, J. Y.; Lu, Y. M.; Shen, D. Z.; Xu, W.; Zhong, G. Z.; Fan, X. W.; Kong, X. G. *J. Appl. Phys.* **2002**, *92*, 3293–3298.

(7) (a) Jose, R.; Thavasi, V.; Ramakrishna, S. *J. Am. Ceram. Soc.* **2009**, *92*, 289–301. (b) Longo, C.; De Paoli, M.-A. *J. Braz. Chem. Sci.* **2003**, *14*, 889–901.

(8) (a) Bauer, C.; Boschloo, G.; Mukhtar, E.; Hagfeld, A. *J. Phys. Chem. B* **2001**, *105*, 5585–5588. (b) Rensmo, H.; Keis, K.; Lindstrm, H.; Sdegren, S.; Solbrand, A.; Hagfeld, A.; Lindquist, S.-E.; Wang, L. N.; Muhammed, M. *J. Phys. Chem. B* **1997**, *101*, 2598–2601.

(9) Grätzel, M. *Inorg. Chem.* **2005**, *44*, 6841–51.

(10) Hagfeldt, A.; Grätzel, M. *Acc. Chem. Res.* **2000**, *33*, 269.

(11) (a) Kelly, C. A.; Meyer, G. J. *Coord. Chem. Rev.* **2001**, *211*, 291–315. (b) Meyer, G. J. *J. Chem. Educ.* **1997**, *74*, 652–656. (c) Guldi, D. M. *J. Phys. Chem. B* **2005**, *109*, 11432–11441.

(12) Kalyanasundaram, K.; Grätzel, M. *Coord. Chem. Rev.* **1998**, *177*, 347–414.

(13) Papageorgiou, N.; Barbé, C.; Grätzel, M. *J. Phys. Chem. B* **1998**, *102*, 4156–4164.

(14) Grätzel, M. *Curr. Opin. Colloid Interface Sci.* **1999**, *4*, 314–321.

(15) Keis, K.; Bauer, C.; Boschloo, G.; Hagfeldt, A.; Westermark, K.; Rensmo, H.; Siegbahn., H. *J. Photochem. Photobiol., A* **2002**, *14*, 57–64.

(16) (a) Martinson, A.; Elam, J.; Hupp, J.; Pellin, M. *Nano Lett.* **2007**, *7* (No. 8), 2183–2187. (b) Law, M.; Greene, L. E.; Radenovic, A.; Kuykendall, T.; Liphardt, J.; Yang, P. *J. Phys. Chem. B* **2006**, *110*, 22652–22663. (c) Galoppini, E.; Rochford, J. *J. Phys. Chem. B* **2006**, *110* (No. 33), 16159–16161.

(17) (a) Chou, T. P.; Zhang, Q.; Fryxell, G. E.; Cao, G. *Adv. Mater.* **2007**, *19*, 2588–2592. (b) Umar, A. *Nanoscale Res. Lett.* **2009**, *4*, 1004–1008.

(18) (a) Keis, K.; Magnusson, E.; Lindstrom, H.; Lindquist, S.-E.; Hagfeldt, A. *Sol. Energy Mater. Sol. Cells* **2002**, *7*, 51–58. (b) Zhang, Q.; Dandeneau, C. S.; Park, K.; Liu, D.; Zhou, X.; Jeong, Y.-H.; Cao, G *J. Nanophotonics* **2010**, *4*, 041540.

(19) Wang, Z. L. *J. Phys.: Condens. Matter* **2004**, *16*, R829–R858.

(20) (a) Okuyama, K.; Lenggoro, I. W. *Chem. Eng. Sci.* **2003**, *58*, 537–547. (b) Park, S. B.; Kang, Y. C. *J. Aerosol Sci.* **1997**, *28*, S473–S474.

(21) Sato, T.; Tanigaki, T.; Suzuki, H.; Saito, Y.; Kido, O.; Kimura, Y.; Kaito, C.; Takeda, A.; Keneko, S. *J. Cryst. Growth* **2003**, *255*, 313–316.

(22) (a) Hong, R. Y.; Shen, Z. H.; Li, H. Z. *Chin. J. Process Eng.* **2005**, *5*, 693–697. (b) Hu, X. L.; Zhu, Y. J.; Wang, S. W. *Mater. Chem. Phys.* **2004**, *88*, 421–426.

(23) (a) Liu, B.; Zeng, H. C. *J. Am. Chem. Soc.* **2003**, *125*, 4430–4431. (b) Zhang, H.; Yang, D.; Ji, Y.; Ma, X. Y.; Xu, J.; Que, D. L. *J. Phys. Chem. B* **2004**, *108*, 3955–3958.

(24) (a) Harnack, O.; Pacholski, C.; Weller, H.; Yasuda, A.; M., J.; Wessels, J. M. *Nano Lett.* **2003**, *3*, 1097–1101. (b) Meulenkamp, E. A. *J. Phys. Chem. B* **1998**, *102*, 5566–5572. (c) Pacholski, C.; Kornowski, A.; Weller, H. *Angew. Chem., Int. Ed.* **2002**, *41*, 1188–1191. (d) Spanhel, L.; Anderson, M. A. *J. Am. Chem. Soc.* **1991**, *113*, 2826–2833. (e) Verges, M. A.; Mifsud, A.; Serna, C. J. *J. Chem. Soc. Faraday Trans.* **1990**, *86*, 959–965. (f) Segets, D.; Gradl, J.; Klupp Taylor, R.; Vassilev, V.; Peukert, W. *ACS Nano* **2009**,

3, 1703–1710. (g) Voigt, M.; Klaumützer, M.; Thiem, H.; Peukert, W. *J. Phys. Chem. C* **2010**, *114*, 6243–6249.

(25) (a) Liu, B.; Zeng, H. C. *Langmuir* **2004**, *20*, 4196–4204. (b) Li, W. J.; Shi, E. W.; Zhong, W. Z.; Yin, Z. W. *J. Cryst. Growth* **1999**, *203*, 186–196. (c) Cheng, B.; Shi, W.; Russell-Tanner, J. M.; Zhang, L.; Samulski, E. T. *Inorg. Chem.* **2006**, *45* (No. 3), 1208–1214.

(26) (a) Zhou, X.; Xie, Z.-X.; Jiang, Z.-Y.; Kuang, Q.; SZhang, S.-H.; Xu, T.; Huang, R.-B.; Zheng, L.-S. *Chem. Commun.* **2005**, 5572–5574. (b) Wang, Z. L.; Kong, X. Y.; Ziuo, J. M. *Phys. Rev. Lett.* **2003**, *91*, 185502. (c) Hsieh, C. H. *J. Chin. Chem. Soc.* **2007**, *54*, 31–34.

(27) Ito, S.; Makari, Y.; Kitamura, T.; Wadab, Y.; Yanagida, S. *J. Mater. Chem.* **2004**, *14*, 385–390.

(28) (a) Saito, M.; Fujihara, S. *Energy Environ. Sci.* **2008**, *1*, 280–283. (b) Hagfeldt, A.; Ojamae, L.; Persson, P. *J. Phys. Chem. B* **2002**, *106*, 10102–10107. (c) Zhang, Q.; Chou, T. P.; Russo, B.; Jenekhe, S. A.; Cao, G. *Angew. Chem., Int. Ed.* **2008**, *47*, 2402–2406.

(29) Gradl, J.; Peukert, W. *Chem. Eng. Sci.* **2009**, *64*, 709–720.

(30) West, A. R. *Solid State Chemistry and Its Applications*; John Wiley & Sons: New York, 1984; pp 174−175.

(31) Sakohara, S.; Ishida, M. *J. Phys. Chem. B* **1998**, *102*, 10169–10175.

(32) Max, J.-J.; Chapados, C. *J. Phys. Chem. A* **2004**, *108*, 3324–3337.

(33) Bottger, G. L.; Geddes, A. L. *Spectrochim. Acta* **1965**, *21*, 1701–1708.

(34) (a) Hong, R. Y.; Qian, J. Z.; Cao, J. X. *Powder Technol.* **2006**, *163*, 160. (b) Kwon, Y. J.; Kim, K. H.; Lim, C. S.; Shim, K. B. *J. Ceram. Process. Res.* **2002**, *3*, 146.

(35) (a) Marczak, R.; Werner, F.; Gnichwitz, J.-F.; Hirsch, A.; Guldi, D. M.; Peukert, W. *J. Phys. Chem. C* **2009**, *113*, 4669–4678. (b) Wong, E. M.; Bonevich, J. E.; Searson, P. C. *J. Phys. Chem. B* **1998**, *102*, 7770–7775.

(36) Marczak, R.; Segets, D.; Voigt, M.; Peukert, W. *Adv. Powder Technol.* **2010**, *21*, 41–49.

(37) (a) Ma, J.; Jiang, C.; Xiong, Y.; Xu, G. *Powder Technol.* **2006**, *167*, 49–53. (b) Hu, Z.; Oskam, G.; Searson, P. C. *J. Colloid Interface Sci.* **2003**, *263*, 454–460.

(38) (a) Viswanatha, R.; Amenitsch, H.; Sarma, D. D. *J. Am. Chem. Soc.* **2007**, *129*, 4470–4475. (b) Viswanatha, R.; Santra, P. K.; Dasgupta, C.; Sarma, D. D. *Phys. Rev. Lett.* **2007**, *98*, 255501/1–255501/4.

(39) (a) Hu, Z.; Herrera Santos, J. F.; Oskam, G.; Searson, P. C. *J. Colloid Interface Sci.* **2005**, *288*, 313–316. (b) Hu, Z.; Oskam, G.; Penn, R. L.; Pesika, N.; Searson, P. C. *J. Phys. Chem. B* **2003**, *107*, 3124–3130.